Diffuse midline glioma invasion and metastasis rely on cell-autonomous signaling

Marco Bruschi, Lilia Midjek, Yassine Ajlil, Stephanie Vairy, Manon Lancien, Samia Ghermaoui, Thomas Kergrohen, Maite Verreault, Ahmed Idbaih, Carlos Alberto Oliveira de Biagi, et al.

Neuro-Oncology

26(3), 553–568, 2024 | https://doi.org/10.1093/neuonc/noad161 | Advance Access date 13 September 2023

Diffuse midline glioma invasion and metastasis rely on cell-autonomous signaling

Marco Bruschi, Lilia Midjek, Yassine Ajlil†, Stephanie Vairy†, Manon Lancien†, Samia Ghermaoui, Thomas Kergrohen, Maite Verreault, Ahmed Idbaih, Carlos Alberto Oliveira de Biagi Junior, Ilon Liu, Mariella G. Filbin, Kevin Beccaria, Thomas Blauwblomme, Stephanie Puget, Arnault Tauziede-Espariat, Pascale Varlet, Volodia Dangouloff-Ros, Nathalie Boddaert, Gwenael Le Teuff, Jacques Grill, Guillaume Montagnac, Nadia Elkhatib, Marie-Anne Debily, and David Castel

All author affiliations are listed at the end of the article

Corresponding Authors: David Castel, Gustave Roussy U981 - B2M, 114 Rue Edouard Vaillant, 94805 Villejuif, France (david.castel@gustaveroussy.fr); Marco Bruschi (marco.bruschi@gustaveroussy.fr), Inserm U981, Molecular Predictors and New Targets in Oncology, Team Genomics and Oncogenesis of Pediatric Brain Tumors, Gustave Roussy, Université Paris-Saclay, Villejuif, France.

†These authors contributed equally.

Abstract

Background. Diffuse midline gliomas (DMG) are pediatric tumors with negligible 2-year survival after diagnosis characterized by their ability to infiltrate the central nervous system. In the hope of controlling the local growth and slowing the disease, all patients receive radiotherapy. However, distant progression occurs frequently in DMG patients. Current clues as to what causes tumor infiltration circle mainly around the tumor microenvironment, but there are currently no known determinants to predict the degree of invasiveness.

Methods. In this study, we use patient-derived glioma stem cells (GSCs) to create patient-specific 3D avatars to model interindividual invasion and elucidate the cellular supporting mechanisms.

Results. We show that GSC models in 3D mirror the invasive behavior of the parental tumors, thus proving the ability of DMG to infiltrate as an autonomous characteristic of tumor cells. Furthermore, we distinguished 2 modes of migration, mesenchymal and ameboid-like, and associated the ameboid-like modality with GSCs derived from the most invasive tumors. Using transcriptomics of both organoids and primary tumors, we further characterized the invasive ameboid-like tumors as oligodendrocyte progenitor-like, with highly contractile cytoskeleton and reduced adhesion ability driven by crucial over-expression of *bone morphogenetic pathway 7 (BMP7)*. Finally, we deciphered MEK, ERK, and Rho/ROCK kinases activated downstream of the BMP7 stimulation as actionable targets controlling tumor cell motility.

Conclusions. Our findings identify 2 new therapeutic avenues. First, patient-derived GSCs represent a predictive tool for patient stratification in order to adapt irradiation strategies. Second, autocrine and short-range BMP7-related signaling becomes a druggable target to prevent DMG spread and metastasis.

Key Points

1 DMG survival is modulated by variable infiltration and metastatic progression.

2 Variable invasiveness relies on stem cell-autonomous mechanisms that are recapitulated by patient-derived GSC models in 3D.

3 GSC motility is promoted by druggable signaling.

Graphical Abstract

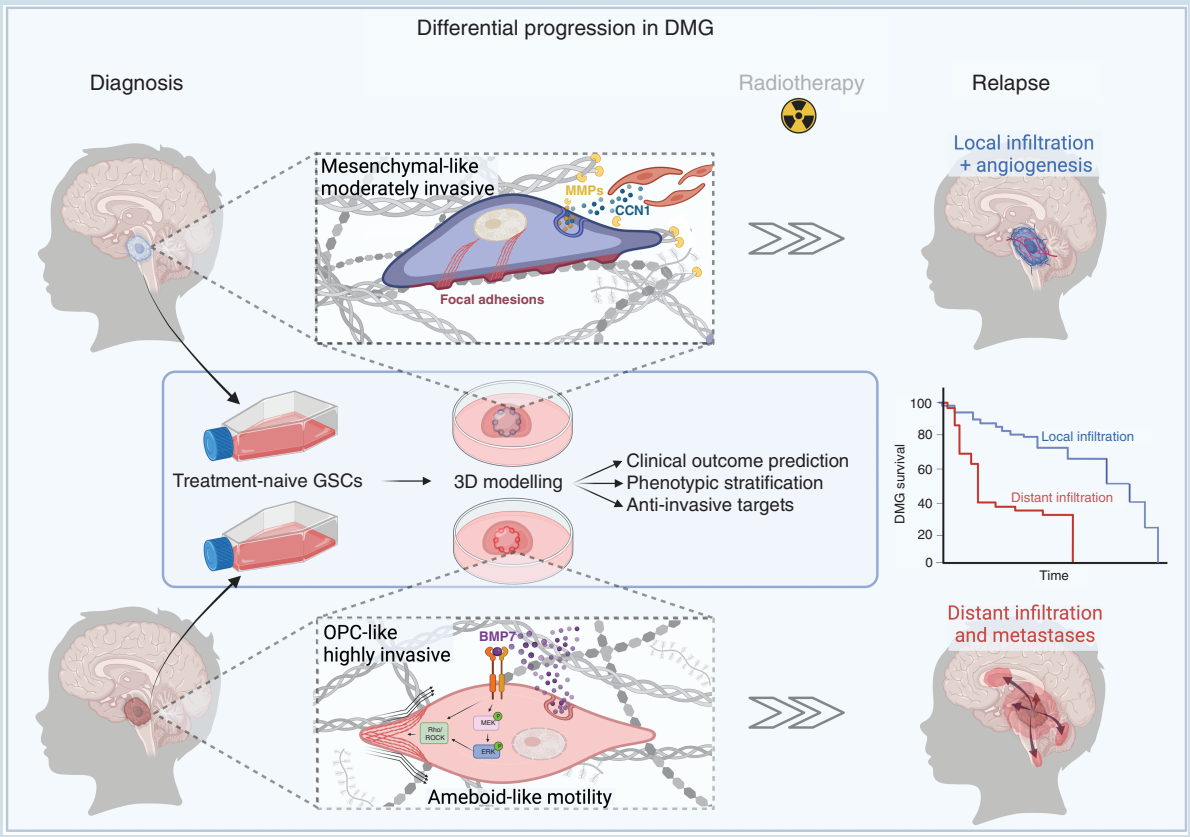

Importance of the Study

This work demonstrates that variable infiltration and metastatic evolution critically affect the prognosis of patients with diffuse midline gliomas (DMGs). Genetic alterations in the tumors cannot predict this evolution accurately. We therefore used 3D patient-derived glioma stem cell (GSC) avatars to measure invasive capacities, which correlated robustly with the appearance of distant intra-CNS metastases. This suggests an important role of GSC-autonomous mechanisms for DMG dissemination. We demonstrate in vitro and in patients that DMGs can be classified into 2 major phenotypic entities defined by distinct expression profiles related to invasion. Moreover, we identified the cell-autonomous BMP7-related signaling as a major regulator of GSC motility and invasion controlling a switch between 2 migration modalities. These findings are clinically relevant, as we demonstrate that kinases activated downstream of *BMP7* represent relevant targets to prevent tumor infiltration, which may allow to design of more effective therapeutic strategies.

Diffuse midline gliomas (DMGs) are highly infiltrative and radio-resistant pediatric cancers with a median survival of just 9 months after diagnosis.These cancers are initiated in the midline, ie, either in the pons (diffuse intrinsic pontine glioma or DIPG), in the thalamus, or in the spine. Over four-fifths of DMG patients have a specific K27M mutation either in the canonical *H3C1/H3C2* (H3.1-K27M) or in the alternative histone H3 variant *H3-3A* (H3.3-K27M). H3.1-K27M and H3.3-K27M mutations determine the 2 main DMG molecular subgroups and the latter is associated with more frequent metastatic progression.[1–4] In all subtypes, the root genetic alteration disrupts the polycomb repressive complex 2 activity, therefore profoundly altering the epigenetic and transcriptional landscapes of tumor cells.[5,6]

Despite recent advances in understanding its molecular etiology, DMG remains incurable. DMGs are phenotypically heterogeneous neoplasia whose progression is associated with specific combinations of recurrent somatic alterations.[7] The intrinsic infiltrative nature of DMG, which precludes any surgical resection, is considered as one of the main aspects contributing to the poor prognosis associated with the disease, as well as, a major obstacle for

the design of effective treatments.[8–10] Locoregional spread through anatomical structures next to the pons is associated with a plethora of neurological effects and related symptoms.[11] Moreover, distant infiltration can lead to the formation of metastatic *foci* in the entire central nervous system.[8,12–15] Past studies on the complex mechanisms driving DMG invasion have mainly focused on the role of the tumor microenvironment in promoting invasion. Indeed, cell chemoattraction was shown to orientate invasion towards specific brain regions.[16] More recently, intratumor genetic heterogeneity was proposed to underlie some form of cooperativity between co-existing tumor clones, in which minor tumor populations instruct other tumor cells to infiltrate.[17] Yet, it is unclear whether these alterations, retrieved in a very limited number of patients, illustrate general druggable mechanisms driving DMG invasiveness.

Glioma stem-like cells (GSCs) are considered the main population responsible for the malignant properties associated with gliomas.[18] This is especially true in the case of DMG, in which polycomb repressive complex 2 inactivation impairs differentiation and promotes the accumulation of stem-like tumor cells with progenitor identity, to ultimately comprise up to 80% of the tumor.[19] Patient-derived GSCs faithfully model the heterogeneous response to chemotherapy[20] or radiotherapy,[21] and recapitulate DMG tumor infiltration when xenografted.[22,23] As such, GSCs may represent a key resource to study DMG invasiveness. However, due to the limited number of available DMG patient-derived models, none have examined the interindividual heterogeneity and underlying cues of variable tumor infiltration.

Here, we characterized classes of tumor invasion and their association with patient survival. We then used original patient-derived 3D avatars to model interindividual infiltration and dissect the cellular mechanisms responsible for invasion in DMG.

Material and Methods

Additional information and all extended methods can be found in Supplementary Methods.

Clinical Cohort, Magnetic Resonance Imaging, and Immunohistological Analysis of Angiogenesis.

Patients were diagnosed between 2007 and 2017. Tumor samples were stereotactically collected at diagnosis in "Necker-Enfants Malades" hospital (Paris, France) and blood DNA was banked under informed consent as previously described.[23] Different tumor portions were dissociated, snap-frozen, or formalin-fixed for histomolecular analyses. H3K27M mutation was confirmed in all patients by DNA sequencing and immunohistochemistry (Supplementary Figure S7). To investigate infiltration and metastasis, we analyzed radiological, histological, clinical, and available genomic data (Supplementary Figure S7). Patients were only considered if: (1) they had available MRI throughout the clinical course of the disease, and (2) these were obtained preferentially with T2-weighted or T2-FLAIR sequences. There was a total of 72 informative patients. MRI were reviewed by 2 independent oncologists and underwent a consensus review in case of disagreement. For the evaluation of parenchymal remodeling and cerebral blood flow, contrast enhancement was categorized as previously described.[4,24] Neo-angiogenesis was determined on IHC from 22 tumors by an experienced neuropathologist.

Survival Analysis

Survival from the date of the diagnosis was correlated with the type of evolution (local-to-locoregional progression vs. metastatic), by using the Kaplan–Meier method and log-rank test. A multivariable Cox regression model was used to evaluate the association of several variables with survival—defined from the date of diagnosis to death, whatever the cause.

2D Cell Culture, shRNA-Mediated Knock-down and Drugs' Evaluation on Proliferation

Patient-derived cultures (DMG and aGB) were developed from fresh tissue as previously reported, cultured on laminin-coated (Gibco-23017015) plasticware, and maintained as previously described.[23] Media are detailed Supplementary Methods. Human nonmalignant OPCs (36055-22 Celprogen) were cultured in a dedicated expansion medium (M36055-22 Celoprogen). Transduction of control- and *BMP7*-shRNAs was achieved as previously described.[21] Inhibitors, or vehicle DMSO (Merck), were added using the D300E digital dispenser (TECAN). Cell proliferation was followed for 5 days after treatment by video-microscopy with an Incucyte S3 (Sartorius) and cell-confluence analysis.

3D-Invasion Assay, Transwell, and 2D Migration Assay

In total, 20 000 early passage (P2 to P6) GSCs were seeded and grown in ultra-low adherence 96-well plates (PrimeSurface-9096UZ) for 48 hours and embedded in Matrigel (Corning-356234). Segmentation of images was performed 0, 24, and 40 hours post-embedding by 2 independent investigators by manually delimitating the gliomaspheres ($n > 4$) using Fiji software. The impact of *BMP7*-knock-down and inhibitors of BMP7-related signaling on invasion was similarly assessed using the Incucyte "3D Tumor Spheroid Assay" (Sartorius). Transwell migration assay was performed with the Incucyte clearview system (Sartorius-4582). 2D migration assays were performed on laminin-coated glass plates in GSC complete medium in the presence/absence of human recombinant BMP7 (Bio-Techne-354BP) and imaged every 20 minutes for 20 hours with an epifluorescence live-microscope. Cells velocities and spread were manually measured using the ImageJ chemotaxis tool (Ibidi).

3D Tumor-Organoids Culture

Culture of tumor-organoids was essentially performed as previously described[25] by embedding 15 000 low-passage dissociated cells in Matrigel (Corning-356234). Tumoroids were cultured for 21 days with complete GSC medium renewed twice a week and pooled ($n > 12$) before RNA extraction.

NGS and ReAnalysis of Single-Cell RNA-Seq Data

Nucleic acid extractions were performed using the Allprep DNA/RNA minikit (Qiagen) for tissue samples, or the Direct-zol isolation kit (Zymo-R2050) with TRIzol (Gibco) for 3D-GSC models according to manufacturer instructions. After library preparation, 100 bp Paired-end reads were generated on an Illumina NovaSeq by IntegraGen SA (Evry, France). Principal component- and differential gene expression analyses were performed with the DESeq2 package. DMG single-cell RNA-seq data were processed as previously published and interrogated for expression of *BMP7* across different previously described malignant cell populations using the package Seurat.[26] Allen brain map single-nucleus transcriptomes from postmortem human brain specimens were interrogated using an in-house pipeline to study *BMP7* expression. Whole-exome sequencing was performed by IntegraGen SA and analyzed as previously described.[27]

GSC Immunofluorescence Staining

For focal adhesion, cytoskeleton, and phospho-SMADs stainings, GSC on laminin-coated plates were fixed with 4% paraformaldehyde, permeabilized with 0.1% triton/PBS for 10 minutes before labeling Vinculin (MERCK-cloneVIIF9), Actin (Tebu-Bio- SC001) or phospho-SMAD (CST-13820) with specific fluorescent probes and imaging with a Thunder epifluorescence microscope (Leica).

RT-qPCR

After reverse transcription of 250–500 ng of total RNA, real-time quantification was performed in triplicate with a ViiA 7 System (ThermoFisher Scientific) on 10 ng of cDNA. Results were analyzed with the 2-ΔΔCt method using *TBP* as reference loading control gene.

Immunoblotting

Proteins were extracted using the RIPA lysis buffer (Cell Signaling Technologies) supplemented with protease and phosphatase inhibitor cocktails (Roche). Proteins were quantified with a BCA kit (ThermoFisher-23225), before electrophoresis of 30 µg of crude extracts on 4%–20% gradient Mini-protean TGX gels (Bio-Rad) and transferred on PVDF membranes (Bio-Rad). Detection of total epitopes was performed as a loading control to evaluate relative phosphorylation. The list of antibodies used is detailed in Supplementary Methods.

Statistical Analysis of Biological Data

Descriptive univariate and multivariate statistics were performed with Graphpad (Version 9.0). Results are plotted as histograms or curves representing means as center values and standard error of the mean as error bars for each experimental group or condition, except when $n < 4$, in which case individual data points were plotted. (*), (**), and (***) indicate P-values < .05, <.01, and < .001, respectively.

Results

DMG Prognosis Depends on Invasion Rate and Metastatic Relapse

We first aimed to determine the impact of invasion on the survival of H3-K27M DMG. We thus evaluated the correlation, between survival and the extent of tumor infiltration, in a cohort of 72 DMG patients. By analyzing matched magnetic resonance imaging (MRI) at diagnosis and at relapse after irradiation, we defined 3 major radiological classes. During follow-up, infiltration occurred locally and remained restricted to the pons in 34% of patients (25/72, Figure 1A), proceeded loco-regionally to extrapontine structures in 42% of patients (30/72), and gave rise to one or multiple distant intracranial or spinal metastases in 24% of patients (17/72). For 3 of the thirty patients with initial local-to-locoregional spread, metastatic evolution occurred at later stages of the disease, leading to a total of 20/72 (28%) patients with metastatic progression at the last follow-up. Metastasis represented an adverse prognostic factor at the time of relapse by univariate analysis, ($P = .003$, Log-rank test; Figure 1B). We therefore performed a multivariate analysis considering progression, either local-to-locoregional or metastatic, as a time-dependent variable (Supplementary Table S1). This confirmed that metastasis significantly reduces survival (HR = 3.64, chi-square $P < .001$), independently of other well-known adverse prognostic factors, such as H3.3-K27M mutation (HR = 2.280, $P = .0231$) and *TP53* mutation status (HR = 2.325, $P = .0057$). The different progression patterns were not related to gender or age at diagnosis (Supplementary Figure S1A,B).

We next distinguished local and locoregional progression types to better describe non-metastatic invasion. We observed that the classes of infiltration correlated with poor survival after relapse ($P = .0055$, Log-rank test Supplementary Figure S1C). We, therefore, measured the maximal axial, coronal, or sagittal distance of tumor invasion, whichever was the longest, in 18 patients by comparing tumor size in radiological images collected after radiotherapy and at the last MRI after progression. This revealed a significant negative correlation (Pearson $P = .002$) between parenchyma invasion rate and survival (Figure 1C). Together, these data demonstrate that DMG invasion negatively impacts survival. Therefore, preventing extensive invasion may represent an important adjunct to local radiotherapy for the management of DMG.

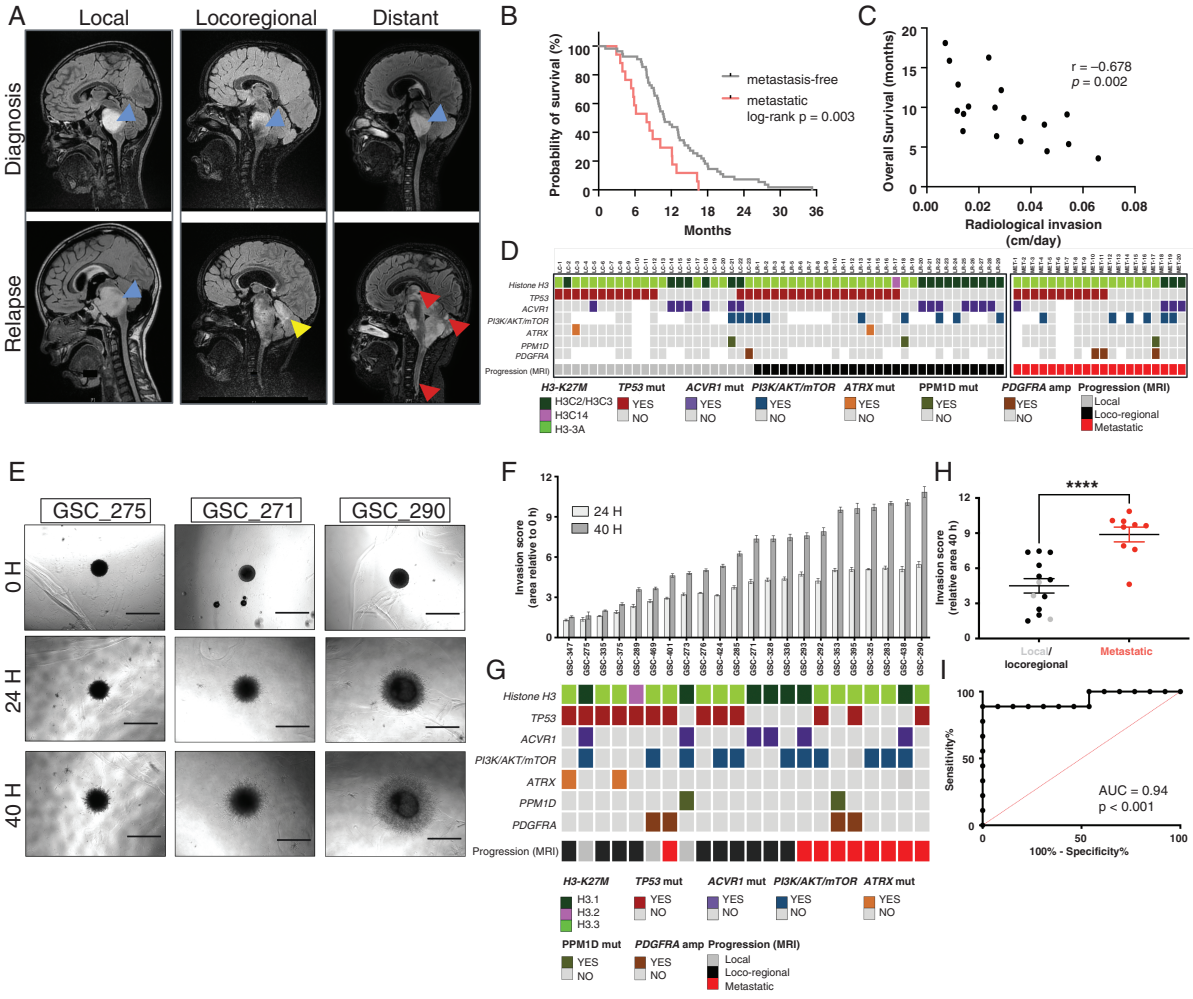

Figure 1. Variable tumor invasion extent correlates with survival and can be recapitulated by glioma stem cell (GSC) models in 3D. (A) Sagittal magnetic resonance images of 3 representative Diffuse midline gliomas (DMG) patients collected at diagnosis (top panels) and progression (bottom panels) displaying from left to right local, extensive locoregional (arrowheads indicate contiguous locoregional infiltration at relapse) and distant relapse (arrowheads indicate metastatic foci); initial pontine localization at diagnosis is pointed by arrowheads. (B) Kaplan–Meier curves of the overall survival (in months) of patients with local-to-locoregional (n = 53) and metastatic (n = 17) progression, according to the radiological assessment at first relapse; 2 patients were excluded as they died without relapse. P-value as by log-rank Mantel-Cox. (C) Overall survival in a cohort of 18 DMG patients with local-to-locoregional tumor evolution, according to the radiological invasion rate, assessed from 2 consecutive MRIs (P-value as by 2-tailed Pearson test). (D) Oncoplot displaying the mutational landscape for 7 recurrently mutated genes detected by whole-exome sequencing or targeted Sanger sequencing in tumor DNA in a cohort of 72 DMG collected at diagnosis (see methods and Supplementary Figure S6 for details on inclusion); white indicates data unavailable; LC, LR and MET indicate patients with subsequent local, locoregional or anytime-metastatic evolutions, respectively. (E) Representative phase-contrast images of invading gliomaspheres in Matrigel at 0-, 24-, and 40 hours post-embedding (scale bar = 600 µm). (F) Gliomasphere invasion ability was relative to the initial sphere area at 24 (light orange) and 40 hours (dark orange) after embedding. Results are ranked according to the average ± s.e.m. of at least 5 technical replicates per cell model. (G) Oncoplot of gliomaspheres displaying the mutational status obtained from whole-exon sequencing or targeted Sanger sequencing for 7 genes recurrently mutated in DMG. Metastatic progression is represented in red, locoregional progression in black, and local progression in light gray. (H) Comparison of relative gliomasphere area at 40 hours after embedding for models derived from patients with local/locoregional (n = 13) or distant metastatic progression (n = 9); average ± s.e.m is shown for both groups; P-value as by 2-tailed unpaired t-test. (I) ROC analysis of the invasion score measured at 40 hours after embedding in the panel of 22 models. The area under the curve is displayed as a measure of the performance of the assay to predict metastatic evolution (max = 1).

We next analyzed the molecular mechanisms supporting variable invasion by performing DNA sequencing on tumor samples. Surprisingly, none of the most recurrent genetic alterations described in the coding genome in DMG at diagnosis, notably in *TP53*, *ACVR1*, *ATRX*, *PPM1D*, PI3K-pathway or platelet-derived growth factor alpha (*PDGFRA*), displayed specific association with metastatic progression (Figure 1D, Supplementary Figure S1D). We, therefore, concluded that no recurrent genetic alteration is predictive of interindividual DMG invasion capacities and relative risk of metastatic progression.

Metastatic Relapse can be Predicted by 3D *In Vitro* Modeling

In the absence of genetic prediction, we thus sought to model in vitro the interindividual differences in tumor infiltration. For this, we decided to study GSC models derived from biopsies of treatment-naïve tumors at diagnosis. We used a panel of 22 different patient-derived GSC models encompassing the spectrum of infiltration level, molecular, and radiological tumor features described in the previous section (Supplementary Table S2). To monitor invasion rate, we grew the GSC into spheroids, embedded them in Matrigel, and allowed them to invade for 40 hours, ie, a time-lapse shorter than the doubling time of all cell models used.The invasion score was measured as the ratio of spheroid area at 24 or 40 hours relative to post-embedding (0 hours). We observed a remarkable interindividual heterogeneity in invasion capacities at both time-points, reaching a 6-fold difference between the least and the most invasive GSC models at 40 hours (Figure 1E,F, Supplementary Videos S1,S2). ATP-based viability assay and the evolution of gliosphere size across the 4 least- and 4 most-invasive models showed neglectable variability in their growth within 48 hours post-formation in noninvasive conditions, ie, without Matrigel (Supplementary Figure S2A–D). This ruled out a possible influence of variable proliferative rate over invasion. Importantly, heterogeneous invasiveness was not linked to any recurrent DMG alteration in protein-coding regions, including mutations of H3 variants and *TP53* (Figure 1G, Supplementary Figure S2E,F).

Strikingly, the degree of in vitro GSC invasion, at both time-points, correlated with the actual metastatic progression in the corresponding patients (Figure 1F,G). Indeed, biopsy-derived models from patients with metastatic relapse were significantly more invasive than those from patients with local-to-locoregional tumor progression (Student's $P < .001$, Figure 1H). Receiver operating characteristic analysis confirmed that the results of the in vitro 3D-invasion assay were highly predictive of the individual risk of metastatic progression (AUC = 0.94, $P = .0006$; Figure 1I). We observed that a 7.4 area ratio threshold, at 40 hours, predicted metastatic evolution with high sensitivity (89%, 8/9 patients) and optimal accuracy (100% specificity). The robustness of the assay was further assessed by a second investigator, blind to clinical data, and using another batch of Matrigel (Supplementary Figure S2G).The 2 datasets were highly concordant ($r = 0.938$, Spearman $P < .001$, Supplementary Figure S2H–J).

Overall, our results demonstrate that GSCs embedded in an extracellular scaffold recapitulate the invasive capacities of corresponding tumors. This suggests that invasion is primarily driven by cell-autonomous mechanisms representing possible therapeutic targets.

Tumor-Organoids Gene Expression Profiles Distinguish Highly From Moderately Invasive DMG

As the 3D-invasion assay faithfully reproduced the clinical outcome of the disease, we performed expression profiling of patient-derived GSCs grown in 3D. We observed that all GSC models in our panel reached 3D confluency by forming tumor organoids (Figure 2A). Organoids rapidly grew and overcame the normal neurosphere size limit of ~500–1000 µm described without extracellular matrix (ECM) scaffold (Supplementary Figure S3A). We then performed RNA-seq profiling of 22 DMG-organoids and 3 adult glioblastoma (aGB)-organoids grown in the same conditions for 21 days. Expression profiles allowed a fair discrimination of tumor organoids derived from adult and pediatric gliomas (Supplementary Figure S2B). As expected, DMG-derived organoids had increased expression of genes with H3K27 tri-methylated promoters, compared to the aGB-organoids. Notably, we found that pediatric organoids were also relatively enriched for oligodendrocyte progenitor cell (OPC) markers[19] (Supplementary Table S3, Figure S3C). By contrast, aGB-organoids had a more mesenchymal signature than pediatric models (Supplementary Figure S3C). We also observed that gene expression discriminated the 22 DMG organoids as a function of H3 mutational status (Supplementary Figure S3D). Indeed, H3.1-K27M organoids showed overexpression of an astrocytic signature, genes involved in ECM remodeling and pro-angiogenic signatures as compared to H3.3-K27M organoids (Supplementary Figure S3E; GSEA in Supplementary Table S4). These observations accurately recapitulate the phenotypic and molecular stratification previously described for primary DMGs.[4,28]

Unsupervised hierarchical clustering of the DMG organoids highlighted the existence of 2 main clusters, C1 and C2, in the panel of 22 patient-derived tumor organoids (Figure 2B). This clustering pattern clearly correlated with the invasion capacities measured for the corresponding GSCs (Student's $P < .001$; Figure 2C). This suggested that the heterogeneous invasiveness observed in tumors and organoids rely on specific transcriptional programs. Interestingly, the moderately invasive C1 cluster models expressed more epithelial-to-mesenchymal transition regulators, such as *TWIST1* and *TGFB1*, and less epithelial E-cadherin (*CDH1*) (Figure 2D,F). The highly invasive GSCs in cluster C2 were enriched in glutamatergic synaptic receptor components and ion voltage-gated channels-related genes, previously implicated in glioma growth and invasion (Supplementary Figure S3f).[29,30] In addition, the C2 cluster had a pronounced OPC identity (Figure 2F left GSEA plots; Supplementary Table S5), supported by the preferential expression of master genes of OPC specification (Figure 2D, bottom insets). Immunoblotting of extracts from the most- and least invasive cell models confirmed that OPC- and epithelial markers OLIG2 and E-cadherin (CDH1) are highly expressed by the cluster of invasive GSCs (Figure 2E). Altogether, these observations suggest that DMGs comprise 2 different phenotypes: highly invasive OPC-like tumors and moderately invasive mesenchymal tumors. *In vitro*, findings were further confirmed by the analysis of RNA-seq of 17 available matched parental biopsies collected at diagnosis. Indeed, DMG samples from patients with subsequent metastatic progression overexpressed fetal OPC signatures as compared to non-metastatic tumors (Figure 2F, left GSEA). Non-metastatic primary tumors at diagnosis overexpressed mesenchymal markers (Figure 2F, right GSEA). Overall, GSC-derived tumoroids accurately mirror the heterogeneity of DMGs

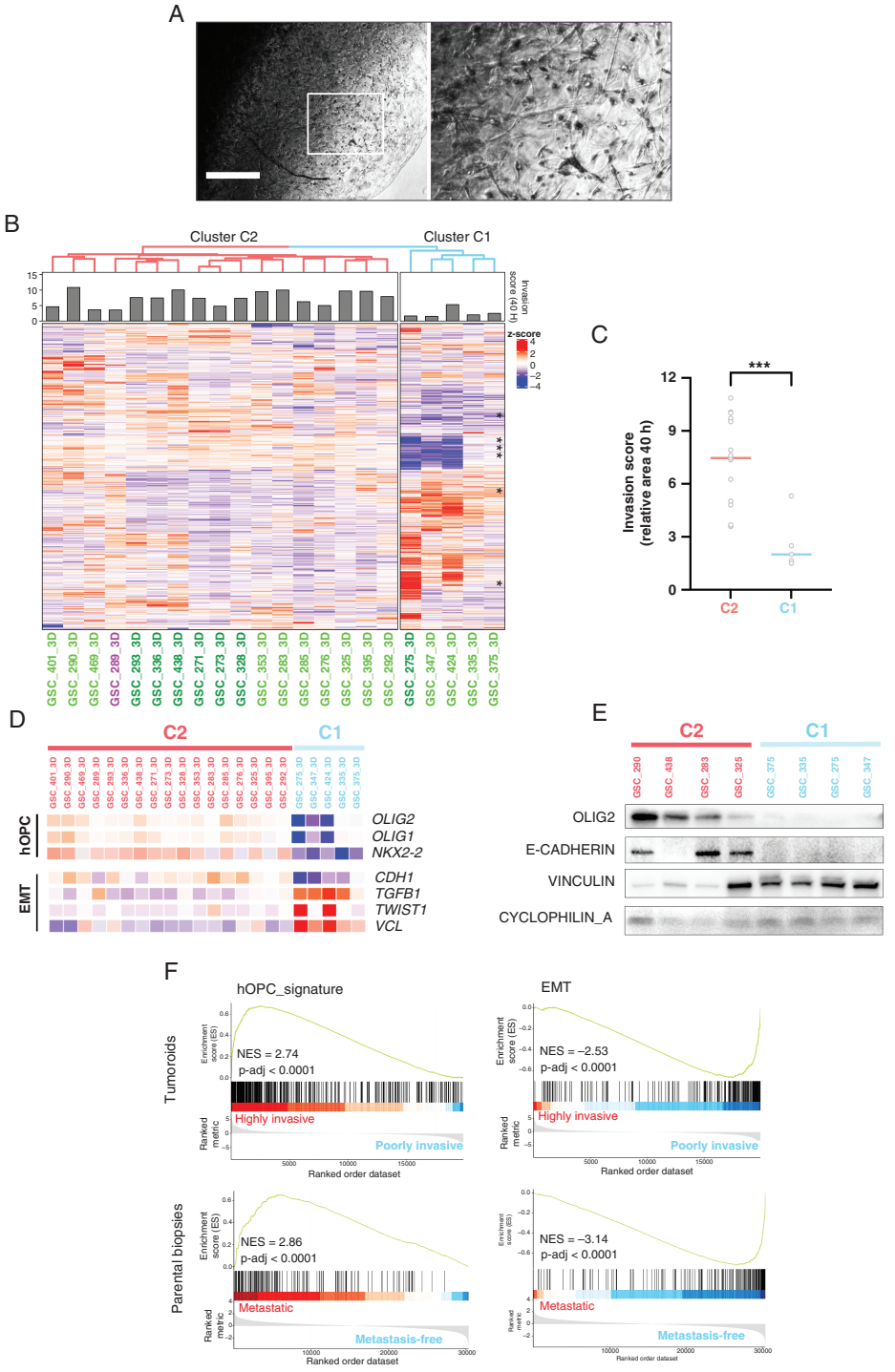

Figure 2. Transcriptomic analysis reveals 2 types of diffuse midline glioma. (A) Representative brightfield and inset images of tumor organoids 10 days after embedding in Matrigel (scale bar = 600µm). (B) Unsupervised hierarchical clustering based on the expression of the 1000 most variable genes, displaying the existence of 2 distinct clusters of Diffuse midline gliomas (DMG) organoids, corresponding to moderately (5 C1 branches) or highly invasive (17 C2 branches) GSC-models; top bars represent the individual relative invasion score 40 hours post-embedding. (C). Relative invasion of glioma stem cells (GSCs) from C1 and C2 clusters measured at 40 hours; results represent average value for each model; *P*-value as by 2-tailed unpaired *t*-test. (D) Magnifications of the heatmap (indicated by * on the general heatmap) highlight the expression patterns of specific markers of oligodendrocyte progenitor cell specification and epithelial-to-mesenchymal transition. (E) Immunoblot on crude protein extracts of the 4 most invasive (red) and 4 least-invasive (blue) GSC models, displaying the detection of hOPC- and mesenchymal protein markers. (F) Gene set enrichment analysis analyses based on the comparison between the 2 molecular clusters of DMG organoids (top plots) or between available profiles of parental biopsies ($n = 17$) from individuals with non-metastatic versus metastatic progression (bottom), suggesting increased oligodendrocyte progenitor cell identity and reduced epithelial-to-mesenchymal transition in invasive 3D-GSC and metastatic samples. Normalized Enrichment Score and Benjamini-Hochberg adjusted *P*-value are shown on the plots; gene sets as by Hallmark and GO-related catalogues.

and gliomas in general, suggesting the existence of 2 different phenotypic entities related to DMG invasion ability.

Differential Cell-Substrate Interaction Modalities Determine DMG Invasive Potential

We next characterized the phenotypic differences between highly and less invasive GSCs. We noticed that the moderately invasive C1 mesenchymal cluster presented enriched expression of genes related to focal adhesion and interaction with the extracellular matrix (Figure 3A, top left and middle panels). RNA-seq of parental tumor biopsies confirmed that focal adhesions and ECM signatures were overrepresented in non-metastatic compared to metastatic DMG at diagnosis (Figure 3A, bottom left and middle panels). Moreover, multiple genes involved in ECM remodeling, including several matrix metalloproteinases, were downregulated in metastatic- compared to metastasis-free DMGs (Supplementary Table S6). In addition, moderately invasive C1 GSCs and parental non-metastatic tumors also over-expressed genes related to sprouting neo-angiogenesis (Figure 3A, right panels). For example, the extracellular positive regulator of angiogenesis *CCN1* ([31]) was upregulated in the C1 cluster compared to the highly invasive C2 cluster (Log2FC = 2.78; adj-$P < .001$, Supplementary Figure S4A). *CCN1* was also upregulated in metastasis-free as compared to metastatic parental DMG biopsies at diagnosis (Log2FC = 2.72; adj-$P < .001$) (Supplementary Figure S4A). Accordingly, T1-weighted contrast enhancement MRI revealed a more intact blood-brain barrier in patients with metastatic evolution as compared to patients with local- (Chi-square $P = .020$) or locoregional progression (Chi-square $P = .016$; Supplementary Figure S4B). Likewise, anatomopathological evaluation on the 22 related biopsies at diagnosis (Supplementary Figure S4C) confirmed an increased endothelial recruitment and proliferation in the least invasive DMGs. Indeed, 3/3 (100%) primary tumors from patients with subsequent local progression were positive compared to 3/10 (30%) tumors with subsequent locoregional—(Chi-square $P = .033$) or 2/9 (22%) metastatic-spread (Chi-square $P = .018$; Supplementary Figure S4D). These structural changes were associated with an increased regional cerebral blood flow at tumor sites at diagnosis, in patients with local progression, compared to tumors with locoregional spread or metastatic evolution (ANOVA $P = .015$ and Anova $P = .003$, respectively; Supplementary Figure S4E,F). Overall, these data suggest that less-invasive gliomas remodel their microenvironment to recruit neo-vessels more than highly invasive gliomas.

To better understand the mechanisms regulating DMG interaction with their microenvironment, we analyzed the adhesion and migration machineries of GSCs in vitro. First, we observed that 2 moderately invasive (C1) patient-derived models morphologically spread efficiently on laminin-coated glass, while 2 highly invasive (C2) GSC lines spanned less on the same substrate (Figure 3B). Quantification of morphological cell spreading area confirmed that C1 and C2 GSCs have different adhesion capacities (Figure 3C). Focal adhesions are integrin-rich structures that ensure strong engagement of the cell with the substrate. We observed that 2 moderately invasive GSCs developed large vinculin-positive focal adhesions (Figure 3B, top panels) that were essentially absent in the 2 highly invasive GSCs. This observation was supported by the RNA-seq and immunoblotting results, showing that Vinculin is overall rarely expressed by the highly invasive models (Figure 2D,E). Focal adhesion formation and maturation are intimately linked to contractile forces exerted by the actin cytoskeleton.[32] We observed numerous actin-stress fibers in the less-invasive GSCs, a characteristic of mesenchymal cells (Figure 3B, bottom panels). Such fibers were mostly absent in highly invasive (C2) GSCs, in which actin rather accumulated in patches at the cell cortex. Live cell imaging of SiR-Actin-labeled GSCs confirmed the presence of numerous, contractile actin stress fibers in the less-invasive cells (Figure 3D, top panels). The expression of mesenchymal signature expressed by C1 tumoroids was therefore corroborated by the presence of large focal adhesions and actin-stress fibers in these cells. Conversely, highly invasive GSCs presented an elongated morphology and an accumulation of actin at the cell rear during migration (Figure 3D, bottom panels). This latter is reminiscent of an ameboid-like migration in which contraction of cortical actin at the rear propels the cell forward.[33] Thus, C1 and C2 GSCs organize their adhesion and migration machineries in drastically different ways. In agreement with 3D-invasion results, we observed that non-adhesive C2 GSCs migrated faster on laminin-coated glass compared to mesenchymal C1 GSCs (Figure 3E). Altogether, our data point to the existence of 2 phenotypically distinct DMG entities that are equipped with different adhesion to the substrate and migration machineries and that variably interact with the microenvironment. This suggests that exacerbated DMG invasion rate is associated with reduced adhesion capacities and with an ameboid-like migration.

Cell-Autonomous and Short-Range Signaling Modulates GSC Invasiveness

To functionally dissect the most relevant cell-autonomous mechanisms and potential regulators modulating DMG infiltration, we selected differentially expressed genes between moderately invasive C1 and highly invasive C2 clusters with an adj-$P < .001$. We also filtered for genes with an elevated positive or negative correlation with the 3D-invasion score. We found 181 differentially expressed genes (63 upregulated and 118 downregulated in the C2 cluster), and 232 genes whose expression level correlated with invasion score measured 40 hours after embedding (76 with Pearson correlation $r > 0.6$ and 156 genes with $r < -0.6$) (Figure 4A). Cross-comparison of the 2 datasets highlighted 40 potential positive or negative regulators of DMG invasion (Figure 4A; Supplementary Table S7).

Intriguingly, among these genes, *bone morphogenetic pathway 7* (*BMP7*) was overexpressed by highly invasive GSCs (log2FC = 5.55, adj-$P < .0001$) and its expression correlated robustly with invasion rate ($r = 0.63$, Pearson $P = .0016$; Figure 4B). BMP7 and BMP4 secretion by astrocytes and brain mesenchymal cell types was previously described as an important cue orchestrating OPC migration

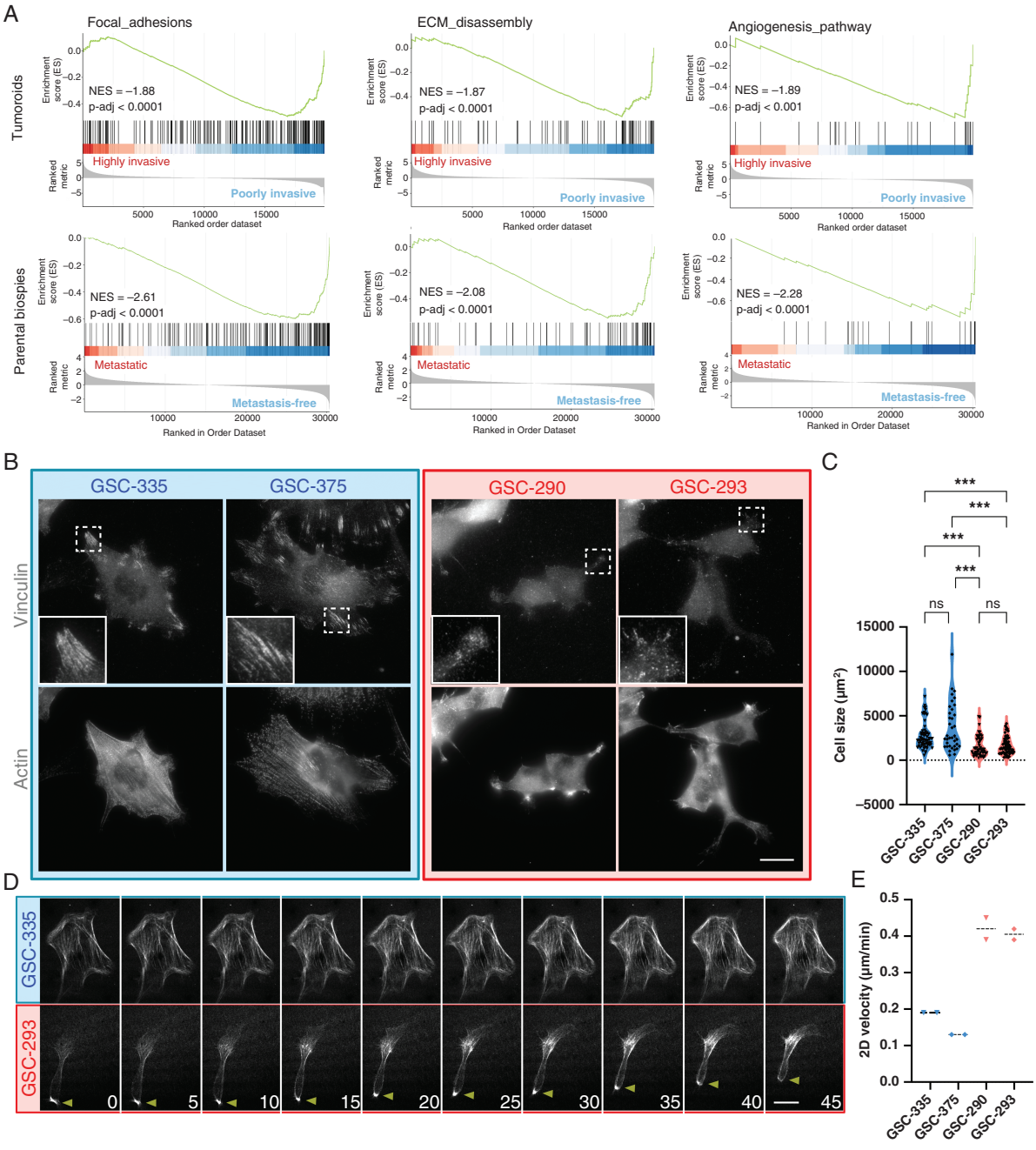

Figure 3. Moderately and highly invasive diffuse midline gliomas cells have distinct actin cytoskeletons and adhesive properties. (A) Gene set enrichment analysis based on the comparison between the 2 molecular clusters of diffuse midline gliomas organoids (top plots) or between available profiles of parental biopsies (n = 17, bottom) from individuals with non-metastatic versus metastatic progression, showing reduced expression of focal adhesion components, extracellular matrix remodeling, and pro-angiogenic signals in invasive 3D-GSC and metastatic tumors. Normalized Enrichment Score and Benjamini–Hochberg adjusted P-values are shown on the plots; gene sets as by Hallmark and GO-related catalogs. (B) The indicated highly- and less invasive glioma stem cells (GSCs) were seeded on laminin-coated glass and then fixed and stained for vinculin (top panels) and F-actin (Phalloidine, bottom panels). Insets show higher magnification of boxed areas. Scale bar: 10 µm. (C) Quantification of moderately (in blue, n = 62 GSC-335, n = 37 GSC-375) and highly invasive GSC (in red, n = 50 GSC-290, n = 63 GSC-375) spread on glass substrate. (D) The indicated GSCs seeded on laminin-coated glass-bottom dishes were incubated for 30 minutes with Sir-Actin before being imaged for 45 minutes with a spinning disk microscope. Galleries of still pictures acquired every 5 minutes are shown. Arrowheads point to actin accumulation at the rear of migrating cells. Scale bar: 10 µm. (E) The indicated GSC models as in (D) were seeded on a laminin-coated glass-bottom dish before they were imaged every 10 minutes for 16 hours. Cell velocity was measured by manual tracking using the Chemotaxis tool of ImageJ; results represent 2 independent experiments with quantification of at least 25 cells per condition.

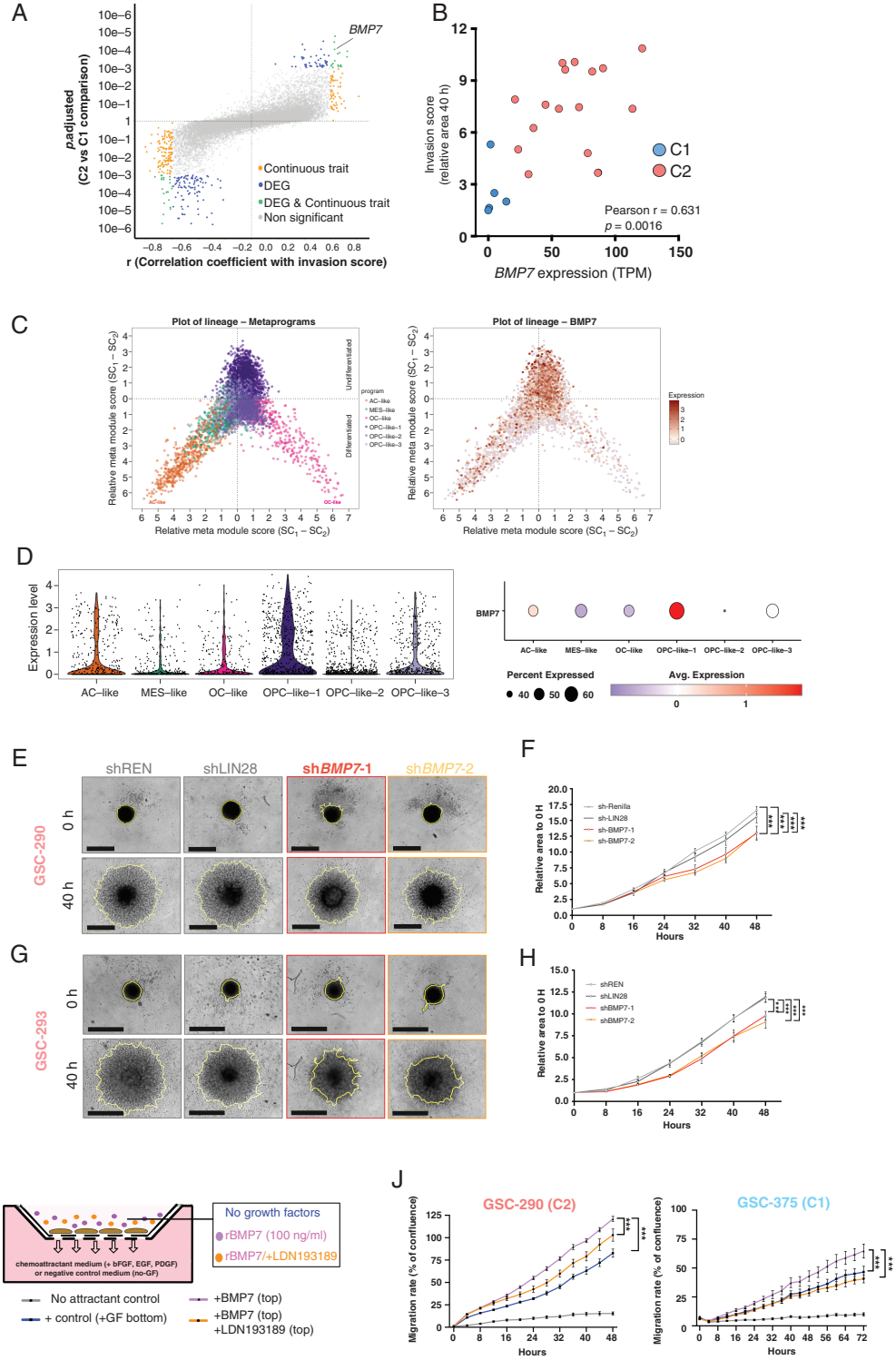

Figure 4. *Bone morphogenetic pathway 7 (BMP7)* expression stimulates invasion in diffuse midline glioma. (A) Scatter plot highlighting differentially expressed genes (adj-$P < 0.01$) between the 2 invasive clusters and those presenting elevated Pearson correlation ($r > 0.55$) with continuous-trait invasive ability; overlap between the 2 is presented as in the color legend. (B) Correlation between *BMP7* RNAseq expression (transcripts per million reads on *x*-axis) and relative invasion score measured at 40 hours in GSCs; *r* and *P*-value as by 2-tailed Pearson correlation. (C) Two-dimensional representations of the OC-like versus AC-like (*x*-axis) and OPC-like (*y*-axis) scores for H3-K27M diffuse midline gliomas cells colored by the different tumor metaprograms (left), or colored according to *BMP7* normalized expression levels as indicated by the color scale (right). This indicates that *BMP7* expression is restricted to the OPC-like metaprogram and to a lesser extent the AC-like program. (D) Violin and dotplot representing the normalized and scaled expression levels of BMP7 across the different tumor cell metaprograms, showing

OPC-like-1 as the prominent cell population expressing *BMP7* (E, G) Live cell microphotographs displaying the invasion of cells after transduction of 2 non-targeting control shRNAs (Renilla, LIN28) and 2 BMP7-specific shRNAs in highly invasive GSC-290 and GSC-293 models; scale bars = 800 µm. (F, H) Quantification of the relative size of gliomaspheres relative to the initial size at embedding over 48 hours; gliomaspheres of 20 000 cells expressing control (Renilla-, Lin28-) or *BMP7*-shRNA; bars represent the average ± s.e.m.; *P*-value as by 2-way ANOVA multiple comparison test. (I) Schematic strategy and (J) results of transwell migration assay performed on highly invasive GSC-290 and moderately invasive GSC-375 patient-derived models in the presence of recombinant BMP7 (100 ng/mL added in the top reservoir) and/or Alk/BMPR inhibitor LDN-193189 (650 nM). Migration is displayed as increasing cell confluence in the bottom compartment over time relative to the initial top confluence. Representative results from 1 out of 2 independent experiments; results represent the average ± s.e.m. of at least 5 technical replicates per condition; *p*-value as by 2-way ANOVA multiple comparison test.

during brain development.[34] BMP4 was very poorly expressed in the cohort of 3D-GSC models (Supplementary Table S7).

Interestingly, by interrogating existing snRNA-seq data in the Allen brain map, we found that *BMP7* expression is mainly associated with OPC and astrocytes in the developing brain (Supplementary Figure S5A,B). These results were strikingly similar to those obtained by reanalysis of recent scRNA-seq data from human pediatric and adult H3-K27M DMGs,[26] where *BMP7* expression is associated with OPC-like tumor cells, especially OPC-like-1 (Figure 4C,D, Supplementary Figure S5D). RT-PCR quantification revealed higher expression of *BMP7* in C2 highly invasive DMG organoids than in normal OPCs (Supplementary Figure S5C). Together, these data suggest that exacerbated *BMP7* expression by GSCs might promote DMG invasion via a cell-autonomous mechanism reminiscent of the OPCs migration during development.

We therefore measured the consequences of RNAi-mediated knock-down on C2 GSC invasion in our 3D assay. Partial but significant knock-down of *BMP7* (Supplementary Figure S5E) significantly delayed the invasion of both *H3C2/H3C3*- and *H3-3A* mutants (Figure 4E–H, Supplementary Videos S3, S4). We confirmed that this was not to be ascribed to a reduction in the growth rate of these models at the timing considered for invasion (Supplementary Figure S5F). In addition, we tested whether exogenous recombinant BMP7 stimulates the migration rate of highly invasive GSC-290. We therefore added rBMP7 together with cells in the top compartment of Transwell migration assay and monitored the translocation towards the chemoattractant-filled bottom compartment (Figure 4I, Supplementary Videos S5). rBMP7 increased the rate of cell migration over time compared to untreated syngeneic GSC. (ANOVA $P < .001$; Figure 4J). Enhanced migration was not a result of increased cell proliferation, as rBMP7 exerted comparable cytostatic effects on highly- and moderately invasive models (Supplementary Figure S5G). This increased migration rate was dependent on BMP type-I receptors, as indicated by the partial reduction of BMP7-induced migration, induced by the pan-Alk inhibitor LDN-193189 (Figure 4I,J). Treatment with rBMP7 also increased the migration rate of less invasive GSCs (GSC-275, -335, and -375) (ANOVA $P < .001$), in a manner dependent on BMP type-I receptor (Figure 4J, Supplementary Figure S5I). Conversely, shRNA-mediated *BMP7* knock-down reduced GSC-290 migration rate (ANOVA $P = .004$; Supplementary Figure S5J). This inhibition was competitively rescued by exogenous rBMP7 (ANOVA $P = .196$). Together, these results strongly support a role for short-range BMP7 signaling as a critical cell-autonomous regulator of DMG invasiveness.

BMP7 Signaling Promotes GSC Invasion by Switching Their Phenotype to Ameboid-Like Migration

The above data demonstrate that *BMP7* expression upregulates invasion of all classes of GSC and the extent of its expression correlates with GSC invasiveness. Importantly, interrogating RNA-seq data by single-sample GSEA showed that mesenchymal identity of individual DMG organoids robustly and inversely correlates with the expression of *BMP7* (Figure 5A; Pearson $r = -0.79$, $P < .001$). This suggested that the auto-paracrine BMP7 signaling might dictate the GSC phenotype and invasiveness independently on the tumor genetic landscape.

We therefore tested the effect of modulating BMP7-related signaling. rBMP7 induced a loss of focal adhesions in C1 GSCs (Figure 5B) and reduced morphological cell spreading on laminin-coated glass (Figure 5C). Exogenous BMP7 also increased the migration velocity of less invasive GSCs on glass (Figure 5D). Conversely, *BMP7* knock-down resulted in the accumulation of focal adhesions in highly invasive GSCs (Figure 5E). Focal adhesion and morphological spreading were abolished when rBMP7 was added back to *BMP7*-knock-down cells (Figure 5E,F). Together, these observations suggest that *BMP7* dictates the organization of the adhesion and migration machineries leading to a switch between a mesenchymal-like to ameboid-like migration.

Migration Modalities are Dictated by BMP7-Induced Kinase Activation

BMP7 was previously reported as an activator of the non-canonical BMP effectors MEK and ERK kinases.[35,36] MEK- and ERK-signaling pathways were shown to regulate normal OPC migration.[37,38] As expected, exogenous rBMP7 rapidly activated the phosphorylation of canonical BMP signaling effectors SMAD1/5/9 in both poorly- and highly invasive models (Figure 6A). This resulted in the nuclear translocation of SMADs (Supplementary Figure S6A). However, baseline translocation in non-stimulated cells was not accentuated in highly invasive models. Importantly, we observed that rBMP7 induced a rapid phosphorylation of MEK and ERK1/2 in both moderately and highly invasive GSC models (Figure 6A). Activation of these MAP-Kinases occurred concomitantly to hyper-phosphorylation of PI3K

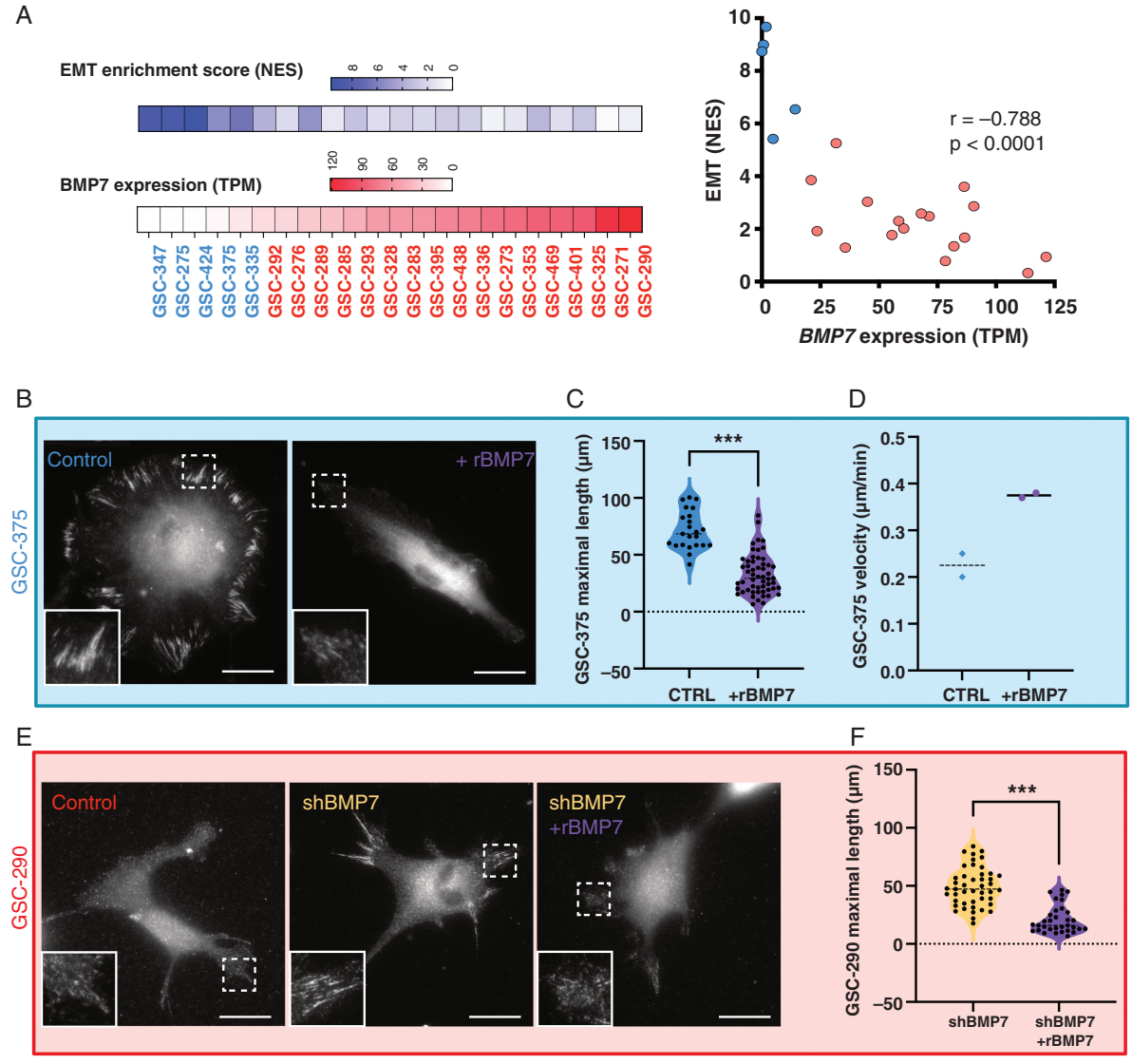

Figure 5. *Bone morphogenetic pathway 7 (BMP7)* regulates a mesenchymal-to-ameboid phenotypic switch. (A) Heatmaps representing the ranked expression of *BMP7* (left) by the 22 3D-GSC models compared to the normalized enrichment in the expression of epithelial-to-mesenchymal transition signature as by single sample gene set enrichment analysis (see methods); scatter plot showing inverse correlation between these 2 traits is represented in the right panel; *r* and *P* as by 2-tailed Pearson correlation. (B) Moderately invasive GSC-375 cells were seeded on laminin-coated glass coverslips and treated (or not) with 100 ng/mL recombinant BMP7 for 24 hours, as indicated, before being fixed and stained for vinculin. Insets show higher magnification of boxed areas. Scale bar: 10 µm. (C) Quantification of the length of cells' long axis cells as in (B). Data are expressed as maximal length in µm of individual cells from 2 independent experiments. (D) Cells as in (B) were seeded on a laminin-coated glass-bottom dish before being imaged every 10 minutes for 16 hours. Cell velocity was measured by manually tracking 60–100 cells per condition over 16 hours using the Chemotaxis tool of ImageJ. (E) shBMP7-expressing highly invasive GSC-290 cells were seeded on laminin-coated glass coverslips and treated (or not) with 100 ng/mL recombinant BMP7 for 24 hours, as indicated, before being fixed and stained for vinculin. Insets show higher magnification of boxed areas. Scale bar: 10 µm. (F), Quantification of the length of cells' longest axis in cells as in (E). Data are expressed as the average of maximal length in µm of individual cells from 2 independent experiments.

and AKT (Figure 6A, Supplementary Figure S6B). However, PI3K/AKT/mTOR activation could only be ascribed to the presence of growth factors and not to BMP7 stimulation, as exogenous BMP7 did not increase the phosphorylation of their downstream target S6. rBMP7 did not substantially alter p38 phosphorylation.

ERK1/2 activation has been shown to regulate the activity of myosin-II, an actin-dependent molecular motor that controls the contractility of the actin cytoskeleton.[39] The RhoA GTPase and its effector Rho-associated protein kinase (ROCK) are also critical regulators of myosin-II activity that were recently shown to functionally interact with ERK to orchestrate cell polarization during migration.[39] Accordingly, rBMP7 increased the phosphorylation of myosin II light chain (Figure 6A). This suggests that the rapid and actionable migration modality switch

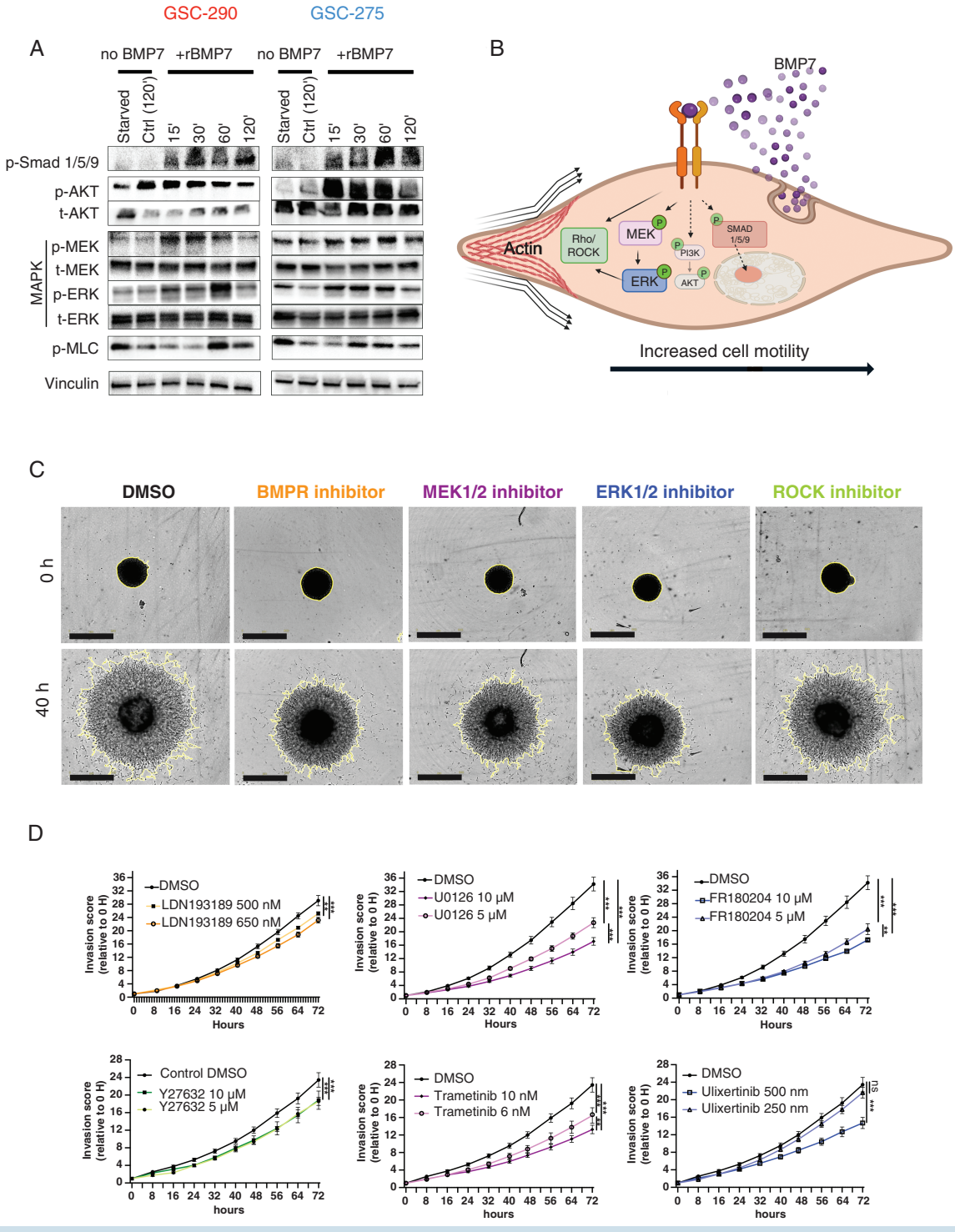

Figure 6. Bone morphogenetic pathway 7 (BMP7) activates a kinase-mediated signaling promoting GSC invasion. (A) Immunoblots performed on GSC_290 (left) and GSC-275 cells (right), after 2 hours of incubation either in medium without any growth factor (starved) or in complete GSC medium without BMP7, or in complete medium with 100 ng/mL recombinant BMP7 for 0, 15, 30, 60, and 120 minutes before harvesting the cells; P = phosphorylated, T = total protein. (B) schematic representation of the signaling cascade activated by secreted BMP7. Interaction of BMP7 with cognate Alk receptors induces the sequential phosphorylation and activation of canonical SMADs, the PI3K/AKT axis, or MAP-kinases MEK and ERK to promote the activity of Rho-GTPase; MAPK activations associated with pro-invasive phenotypic switch and increased cell motility mediated by the actin-mediated propulsion. (C) Representative video-microscopy images 40 hours post-embedding of GSC-290 gliospheres treated with different amounts of LDN-193189, E0126, FR180204, and Y-27632 at embedding; scale bars = 800 µm. (D) Quantification of relative invasion of the different conditions in representative experiments. GSC medium with DMSO at corresponding concentration was used as a control.

described above is activated by BMP7 and may regulate general actin cytoskeleton organization and contractility (Figure 6B). To test this hypothesis, we measured the consequences of MEK, ERK1/2, and ROCK inhibition, as well as of BMP type-I receptors inhibition, in our 3D-invasion assay by using specific drugs at non-cytostatic concentrations (Supplementary Figure S6D). Strikingly, all these inhibitors impaired the invasion rate of highly invasive GSCs in a dose-dependent manner (Figure 6C,D). Importantly, the MEK1/2-inhibitor Trametinib and the ERK1/2-inhibitor Ulixertinib provided comparable results. We confirmed that activation of the pro-invasive signaling cascade was dependent on BMP7 stimulation and its cognate receptors, as selective inhibition of BMPR, MEK or ERK1/2 effectively reduced the hyperphosphorylation of the respective downstream targets in response to exogenous rBMP7 (Supplementary Figure S6C). Moreover, inhibition of BMPR prevented the hyperphosphorylation of canonical SMAD1/5/9, whereas, inhibiting MEK and ERK function did not affect SMAD phosphorylation.

Therefore, GSCs can coopt the BMP7-regulated signaling pathways that orchestrate normal, developmental OPC migration to promote DMG invasion.

Discussion

DMG is among the most aggressive cancers known, afflicting and killing children in short order. Nevertheless, we found that there is a spectrum of severity to the disease and that overall survival inversely correlates with tumor spread and metastatic development. Precision anti-invasive treatment could therefore be key for improved care strategies. Analysis of whole-exome sequencing data showed no recurrent genetic alterations in protein-coding regions to be causative of these events. Although this does not rule out the existence of possible genetic determinants of invasion in the non-coding genome, we searched for alternative phenotypic correlates.

In this work, we made patient-specific GSC-organoids that faithfully mimic tumor behavior and we discerned 2 major modalities of DMG spread. Perhaps surprisingly, the "merely" infiltrative DMGs display a mesenchymal phenotype. This is in sharp contrast with the common assumption that exacerbated mesenchymal phenotype would endow pediatric gliomas with higher infiltrative abilities than adult gliomas.[40] The hyper-invasive DMG we find, are in fact reminiscent of OPCs and display an ameboid-like phenotype. These findings are however consistent with the fact that OPCs are highly motile cells during brain development.[41]

The most intriguing expressed gene differentiating interindividual invasiveness was *BMP7,* a critical microenvironmental regulator of OPC migration during development.[34] Recently, *BMP7* was proposed to induce differentiation in DMG and aGB, therefore reducing their tumorigenic potential.[42,43] The large panel of tumor organoids showed that DMG stem-like cells express *BMP7* at variable extent, and this factor acts as a key regulator of their invasiveness. Interindividual tumor spread is therefore primarily dictated by GSC-autonomous mechanisms.

Mechanistically, we report that *BMP7* expression promotes invasion by reducing focal adhesions and reorganizing the actin cytoskeleton, hence reducing the interaction with the ECM and altering cell contractility and migration. This results in ameboid-like migration, characterized by low adhesion to the substrate and cortical actin contraction at the rear. Such a mesenchymal-to-ameboid switch has already been reported upon artificially inhibiting cancer cell ECM-degradation machinery.[44] However, primary GSCs adopt this migration strategy in response to auto-paracrine *BMP7* expressed by these cells and possibly by their non-neoplastic microenvironment. Specific kinases activated downstream of BMP7, such as MEK, ERK, and ROCK, are interesting therapeutic targets to reduce DMG cell motility. Indeed, inhibitors of these kinases provided promising anti-invasive effects on DMG-derived 3D-GSC. Importantly, Trametinib and Ulixertinib are already approved or under trial for BRAF-altered melanoma, and under consideration for pediatric low-grade gliomas.[45–47] Furthermore, previous preclinical evidences of anti-proliferative effects of Trametinib on DMG cells might imply a possible dual action on growth and dissemination.[48]

Overall, our findings pave the way toward precision stratification strategies for the management of DMG. Currently, almost all patients undergo local irradiation, which is only transiently effective and clearly inadequate for patients with rapid infiltrative spread and metastatic progression. 3D-invasion assay on biopsy-derived GSCs presented here will allow the identification of patients at risk of developing metastasis within weeks post-diagnosis, who might therefore benefit from cranio-spinal irradiation to prevent the appearance of distant *foci*. Moreover, this platform appears robust and sensitive enough to screen compounds or combinations modulating DMG invasion capacities. Improved patient stratification may therefore allow to proposal of adequate care strategies, including treatments specifically targeting cell-autonomous mechanisms of invasion.

Supplementary material

Supplementary material is available online at *Neuro-Oncology* (http://neuro-oncology.oxfordjournals.org/).

Keywords

DMG-H3K27M | GSC | invasion | metastasis | tumor organoids

Funding

Fonds Inkermann funding via the "Fondation de France" (JG, DC, MB). "Etoile de Martin" charity funding (JG, DC, and MAD). "Canceropôle Ile-de-France" and "INCa" grant Emergence no. 2021-1-EMERG-43 (MB), CRIS Cancer Foundation (JG, LM) and the charity "La Marche de l'Ecureuil" (JG).

Acknowledgments

We are grateful to the Necker Imagine DNA biobank (BB-033-00065) and tumor bank, to the Necker operating room nurses/assistants for their technical assistance, to Y. Lecluse from the PFIC core cytometry and microscopy platforms at Gustave Roussy, to I. Leroux (ICM-Paris, France) for advice on the establishment of 3D models, and to J. Pannequin for her advice on the manuscript.

Conflict of interest statement

The authors declare that they have no competing interests.

Authorship statement

M.B., L.M., N.E., S.G., M.L., and A.T.E. performed the experiments. K.B., T.B., and S.P. provided tumor samples. M.B. L.M. N.E. S.V., Y.A., T.K., M.V., A.I., C.A.O.B., I.L., M.G.F., P.V., V.D.R., G.L.T., J.G., M.D. and D.C. analyzed the data. M.B., N.E., G.M., J.G., M.D., and D.C. prepared the manuscript. M.B., J.G. M.D., and D.C. conceived the project. M.B. and D.C. supervised all aspects of the work.

Data availability

All data associated with this study are present in the paper, the supplementary materials, or through publicly accessible domains (https://ega-archive.org). Results related to RNA-seq studies generated from primary tumor samples and GSC models are available under the EGA IDs EGAS00001007181 and EGAS00001007182, respectively.

Affiliations

Inserm U981, Molecular Predictors and New Targets in Oncology, Team Genomics and Oncogenesis of Pediatric Brain Tumors, Gustave Roussy, Université Paris-Saclay, Villejuif, France (M.B., Y.A., S.V., M.L., S.G., T.K., K.B., J.G., M.-A., D.C.); Inserm U1279, Gustave Roussy Institute, Université Paris-Saclay, Villejuif, France (L.M., G.M., N.E.); Département de Cancérologie de l'Enfant et de l'Adolescent, Gustave Roussy, Université Paris-Saclay, Villejuif, France (S.V., J.G.); Sorbonne Université, AP-HP, Institut du Cerveau - Paris Brain Institute - ICM, Inserm, CNRS, Hôpitaux Universitaires La Pitié Salpêtrière - Charles Foix, DMU Neurosciences, Service de Neurologie 2-Mazarin, Paris, France (M.V., A.I.); Department of Pediatric Oncology, Dana-Farber Boston Children's Cancer and Blood Disorders Center, Boston, USA (C.A.O..B., I.L., M.G.F.); Broad Institute of MIT and Harvard, Cambridge, USA (C.A.O..B., I.L., M.G.F.); Department of Pediatric Neurosurgery, Necker Enfants Malades Hospital, APHP, Université Paris Cité, Paris, France (K.B., T.B., S.P.); Department of Neuropathology, GHU Paris-Psychiatrie et Neurosciences, Sainte-Anne Hospital, Paris France (A.T.-E., P.V.); Institut de Psychiatrie et Neurosciences de Paris (IPNP), UMR 1266, INSERM, IMA-BRAIN, Université de Paris, Paris, France (A.T.-E., P.V.); Paediatric Radiology Department, AP-HP, Hôpital Necker Enfants Malades, Université Paris Cité, Institut Imagine INSERM U1163, Paris France (V.D.-R., N.B.); Department of Biostatistics and Epidemiology, Gustave Roussy and Paris-Saclay University, Villejuif, France (G.L.T.); Département de Biologie, Université Evry Paris-Saclay, Evry, France (M.-A.D.)

References

1. Wu G, Broniscer A, McEachron TA, et al; St. Jude Children's Research Hospital–Washington University Pediatric Cancer Genome Project. Somatic histone H3 alterations in paediatric diffuse intrinsic pontine gliomas and non-brainstem glioblastomas. *Nat Genet.* 2012;44(3):251–253.
2. Schwartzentruber J, Korshunov A, Liu X-Y, et al. Driver mutations in histone H3.3 and chromatin remodelling genes in paediatric glioblastoma. *Nature.* 2012;482(7384):226–231.
3. Chan K-M, Fang D, Gan H, et al. The histone H3.3K27M mutation in pediatric glioma reprograms H3K27 methylation and gene expression. *Genes Dev.* 2013;27(9):985–990.
4. Castel D, Philippe C, Calmon R, et al. Histone H3F3A and HIST1H3B K27M mutations define two subgroups of diffuse intrinsic pontine gliomas with different prognosis and phenotypes. *Acta Neuropathol.* 2015;130(6):815–827.
5. Lewis PW, Müller MM, Koletsky MS, et al. Inhibition of PRC2 activity by a gain-of-function H3 mutation found in pediatric glioblastoma. *Science.* 2013;340(6134):857–861.
6. Bender S, Tang Y, Lindroth AM, et al. Reduced H3K27me3 and DNA hypomethylation are major drivers of gene expression in K27M mutant pediatric high-grade gliomas. *Cancer Cell.* 2013;24(5):660–672.
7. Jones C, Baker SJ. Unique genetic and epigenetic mechanisms driving paediatric diffuse high-grade glioma. *Nat Rev Cancer.* 2014;14(10):651–661.
8. Wagner S, Benesch M, Berthold F, et al. Secondary dissemination in children with high-grade malignant gliomas and diffuse intrinsic pontine gliomas. *Br J Cancer.* 2006;95(8):991–997.
9. Wagner MW, Bell WR, Kern J, et al. Diffusion tensor imaging suggests extrapontine extension of pediatric diffuse intrinsic pontine gliomas. *Eur J Radiol.* 2016;85(4):700–706.
10. Kluiver TA, Alieva M, van Vuurden DG, Wehrens EJ, Rios AC. Invaders exposed: understanding and targeting tumor cell invasion in diffuse intrinsic pontine glioma. *Front Oncol.* 2020;10:92. doi:10.3389/fonc.2020.00092
11. Johung TB, Monje M. Diffuse intrinsic pontine glioma: New pathophysiological insights and emerging therapeutic targets. *Curr Neuropharmacol.* 2017;15(1):88–97.
12. Donahue B, Allen J, Siffert J, Rosovsky M, Pinto R. Patterns of recurrence in brain stem gliomas: Evidence for craniospinal dissemination. *Int J Radiat Oncol Biol Phys.* 1998;40(3):677–680.
13. Caretti V, Bugiani M, Freret M, et al. Subventricular spread of diffuse intrinsic pontine glioma. *Acta Neuropathol.* 2014;128(4):605–607.
14. Hoffman LM, DeWire M, Ryall S, et al. Spatial genomic heterogeneity in diffuse intrinsic pontine and midline high-grade glioma: Implications

for diagnostic biopsy and targeted therapeutics. *Acta Neuropathol Commun.* 2016;4(13):1.
15. Nikbakht H, Panditharatna E, Mikael LG, et al. Spatial and temporal homogeneity of driver mutations in diffuse intrinsic pontine glioma. *Nat Commun.* 2016;7:11185. doi:10.1038/ncomms11185
16. Qin EY, Cooper DD, Abbott KL, et al. Neural precursor-derived pleiotrophin mediates subventricular zone invasion by glioma. *Cell.* 2017;170(5):845–859.e19.
17. Vinci M, Burford A, Molinari V, et al. Functional diversity and cooperativity between subclonal populations of pediatric glioblastoma and diffuse intrinsic pontine glioma cells. *Nat Med.* 2018;24(8):1204–1215.
18. Prager BC, Bhargava S, Mahadev V, Hubert CG, Rich JN. Glioblastoma stem cells: Driving resilience through chaos. *Trends Cancer.* 2020;6(3):223–235. Elsevier.
19. Filbin MG, Tirosh I, Hovestadt V, et al. Developmental and oncogenic programs in H3K27M gliomas dissected by single-cell RNA-seq. *Science.* 2018;360(6386):331–335.
20. Grasso CS, Tang Y, Truffaux N, et al. Functionally defined therapeutic targets in diffuse intrinsic pontine glioma. *Nat Med.* 2015;21(6):555–559.
21. Werbrouck C, Evangelista CCS, Lobón-Iglesias M-J, et al. TP53 pathway alterations drive radioresistance in Diffuse Intrinsic Pontine Gliomas (DIPG). *Clin Cancer Res.* 2019;25(22):6788–6800.
22. Monje M, Mitra SS, Freret ME, et al. Hedgehog-responsive candidate cell of origin for diffuse intrinsic pontine glioma. *Proc Natl Acad Sci U S A.* 2011;108(11):4453–4458.
23. Plessier A, Le Dret L, Varlet P, et al. New in vivo avatars of diffuse intrinsic pontine gliomas (DIPG) from stereotactic biopsies performed at diagnosis. *Oncotarget.* 2017;8(32):52543–52559.
24. Calmon R, Dangouloff-Ros V, Varlet P, et al. Radiogenomics of diffuse intrinsic pontine gliomas (DIPGs): Correlation of histological and biological characteristics with multimodal MRI features. *Eur Radiol.* 2021;31(12):8913–8924.
25. Hubert CG, Rivera M, Spangler LC, et al. A Three-dimensional organoid culture system derived from human glioblastomas recapitulates the hypoxic gradients and cancer stem cell heterogeneity of tumors found *In Vivo*. *Cancer Res.* 2016;76(8):2465–2477.
26. Liu I, Jiang L, Samuelsson ER, et al. The landscape of tumor cell states and spatial organization in H3-K27M mutant diffuse midline glioma across age and location. *Nat Genet.* 2022;54(12):1881–1894.
27. Kergrohen T, Castel D, Teuff GL, Tauziède-Espariat A, Lechapt-Zalcman E, Nysom K, et al. Copy-number alterations reshape the classification of diffuse intrinsic pontine gliomas. First exome sequencing results of the BIOMEDE trial [Internet]. medRxiv; 2021. 2021.04.29.21256183. Accessed: March 17, 2023. https://www.medrxiv.org/content/10.1101/2021.04.29.21256183v1
28. Puget S, Philippe C, Bax DA, et al. Mesenchymal transition and PDGFRA amplification/mutation are key distinct oncogenic events in pediatric diffuse intrinsic pontine gliomas. *PlOs One.* 2012;7(2):e30313.
29. Turner KL, Honasoge A, Robert SM, McFerrin MM, Sontheimer H. A proinvasive role for the Ca(2+) -activated K(+) channel KCa3.1 in malignant glioma. *Glia.* 2014;62(6):971–981.
30. Venkatesh HS, Morishita W, Geraghty AC, et al. Electrical and synaptic integration of glioma into neural circuits. *Nature.* 2019;573(7775):539–545.
31. Leu S-J, Lam SC-T, Lau LF. Pro-angiogenic activities of CYR61 (CCN1) mediated through integrins αvβ3 and α6β1 in human umbilical vein endothelial cells *. *J Biol Chem.* 2002;277(48):46248–46255. Elsevier.
32. Gardel ML, Schneider IC, Aratyn-Schaus Y, Waterman CM. Mechanical integration of actin and adhesion dynamics in cell migration. *Annu Rev Cell Dev Biol.* 2010;26:315–333. doi:10.1146/annurev.cellbio.011209.122036
33. Lämmermann T, Sixt M. Mechanical modes of "amoeboid" cell migration. *Curr Opin Cell Biol.* 2009;21(5):636–644.
34. Choe Y, Huynh T, Pleasure SJ. Migration of oligodendrocyte progenitor cells is controlled by transforming growth factor β family proteins during Corticogenesis. *J Neurosci.* 2014;34(45):14973–14983.
35. Liu X, Zhao Y, Peng S, et al. BMP7 retards peripheral myelination by activating p38 MAPK in Schwann cells. *Sci Rep.* 2016;6:31049. doi:10.1038/srep31049
36. Awazu M, Nagata M, Hida M. BMP7 dose-dependently stimulates proliferation and cadherin-11 expression via ERK and p38 in a murine metanephric mesenchymal cell line. *Physiol Rep.* 2017;5(16):e13378.
37. Frost EE, Zhou Z, Krasnesky K, Armstrong RC. Initiation of oligodendrocyte progenitor cell migration by a PDGF-A activated extracellular regulated kinase (ERK) signaling pathway. *Neurochem Res.* 2009;34(1):169–181.
38. Ortega JA, Alcántara S. BDNF/MAPK/ERK-induced BMP7 expression in the developing cerebral cortex induces premature radial glia differentiation and impairs neuronal migration. *Cereb Cortex.* 2010;20(9):2132–2144.
39. Aoki K, Kondo Y, Naoki H, et al. Propagating wave of ERK activation orients collective cell migration. *Dev Cell.* 2017;43(3):305–317.e5.
40. Meel MH, Schaper SA, Kaspers GJL, Hulleman E. Signaling pathways and mesenchymal transition in pediatric high-grade glioma. *Cell Mol Life Sci.* 2018;75(5):871–887.
41. Binamé F, Sakry D, Dimou L, Jolivel V, Trotter J. NG2 regulates directional migration of oligodendrocyte precursor cells via rho GTPases and polarity complex proteins. *J Neurosci.* 2013;33(26):10858–10874.
42. Sachdeva R, Wu M, Johnson K, et al. BMP signaling mediates glioma stem cell quiescence and confers treatment resistance in glioblastoma. *Sci Rep.* 2019;9(1):14569.
43. Sun Y, Yan K, Wang Y, et al. Context-dependent tumor-suppressive BMP signaling in diffuse intrinsic pontine glioma regulates stemness through epigenetic regulation of CXXC5. *Nat Cancer.* 2022;3(9):1105–1122.
44. Wolf K, Mazo I, Leung H, et al. Compensation mechanism in tumor cell migration: mesenchymal-amoeboid transition after blocking of pericellular proteolysis. *J Cell Biol.* 2003;160(2):267–277.
45. Kondyli M, Larouche V, Saint-Martin C, et al. Trametinib for progressive pediatric low-grade gliomas. *J Neurooncol.* 2018;140(2):435–444.
46. Sullivan RJ, Infante JR, Janku F, et al. First-in-Class ERK1/2 Inhibitor Ulixertinib (BVD-523) in Patients with MAPK mutant advanced solid tumors: Results of a phase I dose-escalation and expansion study. *Cancer Discov.* 2018;8(2):184–195.
47. Sigaud R, Rösch L, Gatzweiler C, et al. The first-in-class ERK inhibitor ulixertinib shows promising activity in MAPK-driven pediatric low-grade glioma models. *Neuro Oncol.* 2023;25(3):566–579.
48. Izquierdo E, Carvalho DM, Mackay A, et al. DIPG harbour alterations targetable by MEK inhibitors, with acquired resistance mechanism overcome by combinatorial inhibition. *Cancer Discov.* 2022;2(3):712–729.